General relation between stacking order and Chern index: A topological map of minimally twisted bilayer graphene

S. Theil,[1] M. Fleischmann,[1] R. Gupta,[2] F. Rost,[1] F. Wullschläger,[3] S. Sharma,[4] B. Meyer,[3] and S. Shallcross[4]

[1]*Lehrstuhl für Theoretische Festkörperphysik, Friedrich-Alexander-Universität Erlangen-Nürnberg (FAU), Staudtstr. 7-B2, 91058 Erlangen, Germany*

[2]*H. H. Wills Physics Laboratory, University of Bristol, Tyndall Avenue, Bristol BS8 1TL, United Kingdom*

[3]*Interdisciplinary Center for Molecular Materials (ICMM) and Computer-Chemistry-Center (CCC), Friedrich-Alexander-Universität Erlangen-Nürnberg (FAU), Nägelsbachstraße 25, 91052 Erlangen, Germany*

[4]*Max-Born-Institute for Non-linear Optics and Short Pulse Spectroscopy, Max-Born Strasse 2A, 12489 Berlin, Germany*

(Received 26 June 2020; revised 20 June 2021; accepted 6 July 2021; published 7 September 2021)

We derive a general relation between the stacking vector **u** describing the relative shift of two layers of bilayer graphene and the Chern index. We find $C = \nu(1 - \mathrm{sign}(|V_{\mathrm{AB}}| - |V_{\mathrm{BA}}|))$, where ν is a valley index and $|V_{\alpha\beta}|$ the absolute value of the **u** dependent stacking potentials that uniquely determine the interlayer interaction; AA stacking plays no role in the topological character. With this expression we show that while ideal and relaxed minimally twisted bilayer graphene appear so distinct as to be almost different materials, their Chern index maps are, remarkably, identical. The topological physics of this material is thus strongly robust to lattice relaxations.

DOI: 10.1103/PhysRevB.104.125412

I. INTRODUCTION

Ideal and atomically relaxed twist bilayer graphene becomes, in the small angle regime, essentially different materials [1–5]. While the ideal lattice geometry is that of a moiré, for $\theta < 1^\circ$ the material relaxes ("reconstructs" [3]) into domains of AB and BA stacking bounded by pure screw partial dislocations [6,7]. However, the remarkable electronic properties of the graphene twist bilayer have predominately been established for the ideal geometry [8–14], and a natural question is therefore how the rich electronic physics of the graphene moiré is impacted by the profound lattice relaxation that occurs at small angles [5,15–19].

AB and BA stacked bilayer graphene have different valley Chern numbers, generating a pair of topologically protected states with valley momentum locking at the domain walls of regions of AB and BA stacking. In the ordered network of AB and BA domains that constitute minimally twisted bilayer graphene these one-dimensional states lead to a "helical network" of valley-momentum locked states [20,21] and a remarkable electrically controllable and complete nesting of the Fermi surface [22], with a correspondingly rich magneto-transport that is only beginning to be explored [19,21]. In this paper we will ask the inverse question to that posed above: Can such a network of one-dimensional states be found in the moiré as well as the dislocation network?

Intuitively this may appear unlikely as while the partial dislocation network consists of a mosaic of well defined AB and BA tiles, the ideal moiré geometry does not possess such a bulk/boundary structure. However, as boundary states arise from the change in valley Chern number the possibility exists that, for sufficiently slow stacking modulation, such states exist in the ideal twist geometry through the dependence of the local valley Chern number on the local stacking vector. Remarkably, as we show here, the moiré and the partial dislocation network have essentially identical topological character, in the sense that the spatial dependence of the valley Chern number is indistinguishable between these two systems. This represents an example of a property of the twist bilayer fully robust to lattice relaxation and suggests (i) that the helical network will survive at twist angles when the relaxation to a dislocation network is incomplete and (ii) that in Dirac-Weyl materials for which the energetic balance of in-plane strain and interlayer stacking energy may not favor reconstruction to a dislocation network, the physics of the "helical network" may nevertheless be found.

Our approach will be to generalize the widely known fact that AB and BA stacked bilayer graphene have different valley Chern numbers to a statement concerning an arbitrary stacking vector and the corresponding Chern index. Employing the fact that, under quite general assumptions, the interlayer interaction in bilayer graphene can be represented by three unique "stacking potentials" (corresponding to the three high symmetry stacking types of AB, BA, and AA stacking), we demonstrate that the valley Chern index C depends only on the sign of the difference of the AB and BA potentials as

$$C = \nu - \nu\,\mathrm{sign}(|V_{\mathrm{AB}}| - |V_{\mathrm{BA}}|) \tag{1}$$

with $\nu = \pm 1$ an index labeling the conjugate K valleys. An intervening metallic state is required at a topological phase transition, and we show that the stacking phase diagram of bilayer graphene contains "permanent metal lines" at which the system remains metallic for arbitrary interlayer bias, and that these lines exactly correspond to the stacking vectors at which the valley Chern index changes (Sec. IV). We then numerically investigate the veracity of Eq. (1) through a

series of artificial domain walls for which C is predicted to be different or identical, as well as considering the case of one-dimensional smooth stacking orders looking for bound states associated with a sign change of $|V_{\mathrm{AB}}| - |V_{\mathrm{BA}}|$ (Sec. VI). Finally, we show (Sec. VII) that employing Eq. (1) the topological character of both ideal and relaxed twist bilayer graphene is identical.

II. EFFECTIVE HAMILTONIAN THEORY

To derive the continuum Hamiltonian to be employed in this work we adopt the approach of Ref. [23]. The key to this approach is to consider the tight-binding description of an arbitrary system in terms of a high symmetry system to which a deformation is applied resulting in a generally complex and spatially dependent change in the hopping matrix elements. The relevant two-center tight-binding Hamiltonian can be written as

$$H_{\mathrm{TB}} = \sum_{\substack{\alpha\beta \\ \mathbf{r}\boldsymbol{\delta}}} t_{\alpha\beta}(\mathbf{r}, \boldsymbol{\delta}) c^{\dagger}_{\beta\mathbf{r}+\boldsymbol{\delta}} c_{\alpha\mathbf{r}}. \tag{2}$$

Here α, β represent the combined atomic degrees of freedom of the underlying high symmetry lattice, i.e., layer index, basis atom index, angular momentum, and spin. The function $t_{\alpha\beta}(\mathbf{r}, \boldsymbol{\delta})$ defines the tight-binding hopping matrix element from position $\mathbf{r}$ on sublattice α to position $\mathbf{r} + \boldsymbol{\delta}$ on sublattice β. Note that for graphene in the Hückel tight-binding model (i.e., π-band only) the atomic indices α and β reduce to just the layer and sublattice degrees of freedom.

As shown in Ref. [23] for deformations slow on the scale of the unit cell of the high symmetry system there is a one-to-one relationship between this tight-binding Hamiltonian and continuum Hamiltonian $H(\mathbf{r}, \mathbf{p})$ given by

$$[H(\mathbf{r}, \mathbf{p})]_{\alpha\beta} = \frac{1}{A_{\mathrm{UC}}} \sum_{\mathbf{G}_j} [M_j]_{\alpha\beta}\, \eta_{\alpha\beta}(\mathbf{r}, \mathbf{K}_j + \mathbf{p}), \tag{3}$$

where A_{UC} denotes the area of the unit cell and $\mathbf{G}_j$ are the reciprocal lattice vectors. The sum thus represents the translation group of a conveniently chosen expansion momentum $\mathbf{K}_0$: $\mathbf{K}_j = \mathbf{K}_0 + \mathbf{G}_j$, where in graphene $\mathbf{K}_0$ is chosen to be one of the high symmetry K points of the hexagonal Brillouin zone. The function $\eta_{\alpha\beta}$ is the Fourier transform of the envelope function $t_{\alpha\beta}(\mathbf{r}, \boldsymbol{\delta})$ describing the tight-binding hopping matrix element described above,

$$\eta_{\alpha\beta}(\mathbf{r}, \mathbf{q}) = \int dr\, e^{i\mathbf{q}\cdot\boldsymbol{\delta}} t_{\alpha\beta}(\mathbf{r}, \boldsymbol{\delta}), \tag{4}$$

while the so-called "M matrices" are given by

$$[M_j]_{\alpha\beta} = e^{\mathrm{i}\mathbf{G}_j\cdot(\boldsymbol{\nu}_\alpha - \boldsymbol{\nu}_\beta)}, \tag{5}$$

where the $\boldsymbol{\nu}_\alpha$ denote the basis vectors of the individual sublattices within the unit cell of the underlying high symmetry structure. These matrices encode through the basis vectors $\boldsymbol{\nu}_\alpha$ and reciprocal vectors $\mathbf{G}_j$ the physics of the high symmetry system, while the deformation applied to this high symmetry system, is captured through the spatial dependence of the function $t_{\alpha\beta}(\mathbf{r}, \boldsymbol{\delta})$.

For a high symmetry system, a Taylor expansion in momentum $\mathbf{p}$ of Eq. (3) will generate a series of increasingly accurate Hamiltonians about the expansion point. In graphene the lowest order Hamiltonian will be the Dirac-Weyl equation describing the conical intersection at K, with the higher order terms encoding a series of increasingly accurate low energy approximations to the full band structure [23]. In the presence of deformation fields the layer diagonal blocks of Eq. (3) can also be Taylor expanded for slow deformation to yield the exact single layer tight-binding Hamiltonian plus deformation corrections expressed through (at lowest order) the pseudogauge and spatial variation of the Fermi velocity tensor, as described in Refs. [22,24]. For systems with both intralayer as well as interlayer deformations the electronic structure is dominated by the latter, as shown in Ref. [22], and so we will not include in-plane effective fields here. The dominance of the interlayer deformation arises as while in-plane deformations are restricted by the strong covalent bonding of graphene, interlayer stacking deformations may have essentially arbitrary magnitude (as in a twist deformation) with local stacking varying continuously between the high symmetry types of AA, AB, and BA. As the low energy electronic structure of a bilayer depends profoundly on stacking type (consider the AB as compared to AA spectrum), interlayer deformations are expected to dominate over intralayer deformations in the electronic structure of the bilayer.

Upon applying deformation fields $\mathbf{u}_1(\mathbf{r})$ and $\mathbf{u}_2(\mathbf{r})$ to layers 1 and 2 an interlayer hopping vector $\boldsymbol{\delta}$ will transform as $\boldsymbol{\delta} \to \boldsymbol{\delta} + \mathbf{u}_2(\mathbf{r} + \boldsymbol{\delta}) - \mathbf{u}_1(\mathbf{r})$. For deformation fields varying slowly on the scale of the electron hopping this can be approximated as $\boldsymbol{\delta} \to \boldsymbol{\delta} + \Delta\mathbf{u}(\mathbf{r})$ with $\Delta\mathbf{u}(\mathbf{r}) = \mathbf{u}_2(\mathbf{r}) - \mathbf{u}_1(\mathbf{r})$. The interlayer hopping function is then $t_{\alpha\beta}(\mathbf{r}, \boldsymbol{\delta}) = t^{(0)}_{\alpha\beta}(\boldsymbol{\delta} + \Delta\mathbf{u}(\mathbf{r}))$ with $t^{(0)}(|\boldsymbol{\delta}|)$ the tight-binding hopping function describing the hopping between two π orbitals. The Fourier transform in Eq. (4) can now be performed exactly, yielding a form for the interlayer matrix elements [23]

$$[S(\mathbf{r}, \mathbf{p})]_{\alpha\beta} = \frac{1}{A_{\mathrm{UC}}} \sum_j [M_j]_{\alpha\beta}\, e^{-\mathrm{i}\Delta\mathbf{u}(\mathbf{r})\cdot\mathbf{G}_j}\, t^{(0)}(\mathbf{K}_j + \mathbf{p}) \tag{6}$$

with an explicit dependence on $\Delta\mathbf{u}(\mathbf{r})$, the deformation field describing a local shift of the two layers by $\Delta\mathbf{u}$ at $\mathbf{r}$. For further details we refer the reader to Ref. [23] as well as several applications of the method: to minimally twisted bilayer graphene [22], partial dislocation networks [25–27], and in-plane deformation fields [24,28].

The C_3 symmetry of graphene demands that each star of the translation group of momentum boosts encoded in the above equation is described by the same 3 "M matrices":

$$M_0 = \begin{pmatrix} 1 & 1 \\ 1 & 1 \end{pmatrix}, \qquad M_{\pm} = \begin{pmatrix} 1 & e^{\pm 2\pi\mathrm{i}/3} \\ e^{\mp 2\pi\mathrm{i}/3} & 1 \end{pmatrix} \tag{7}$$

and for this reason the interlayer coupling can be expressed as a sum of three distinct components. The most convenient way to do this is to decompose the interlayer interaction in terms of the three stacking potentials associated with AB, BA, and AA stacking, which have matrix structure σ_+, σ_-, and σ_0, respectively. This then yields a general form for the Hamiltonian of bilayer graphene for arbitrary (spatially varying) interlayer

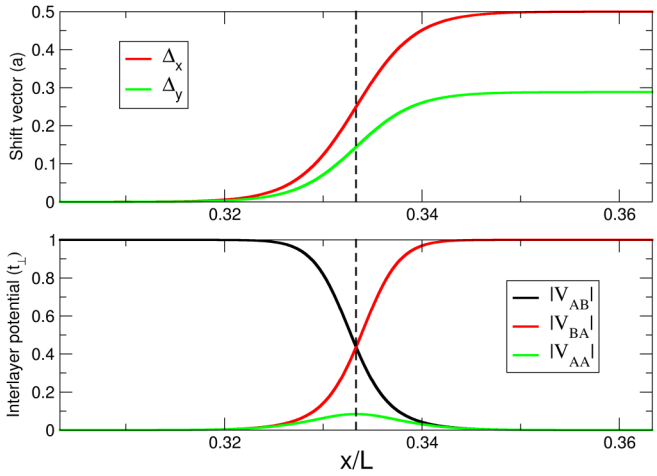

FIG. 1. Shift vector $\Delta\mathbf{u}$ and magnitude of the corresponding interlayer stacking potentials given by Eq. (6) [see also Eq. (8)] for a partial dislocation of partial Burgers vector $a(\frac{1}{2}, \frac{1}{2\sqrt{3}})$ with a the lattice constant of graphene. The interlayer potentials V_{AB}, V_{BA}, V_{AA} reflect the local stacking structure, with a transition from AB to BA stacking seen across the partial dislocation. For detailed discussion of these potentials see Sec. II.

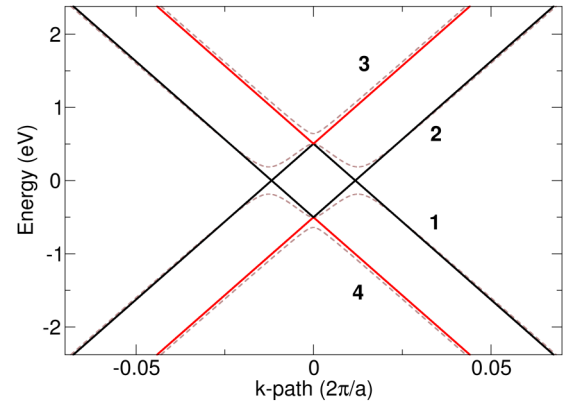

FIG. 2. Full lines: band structure of AB stacked bilayer graphene in the presence of a nonzero interlayer bias but with the interlayer coupling switched off (i.e., no electron hopping between the two layers). The single layer bands indicated by the numbers 1–4 are employed as a basis in the calculations of Sec. III and Sec. IV, with black shaded bands (1 and 2) forming a low energy basis and the red shaded bands (3 and 4) a high energy basis. As described in Sec. III, both the low and high energy sectors are required to obtain the correct valley Chern number for a general stacking. The broken lines represent the band structure of AB stacked bilayer graphene with the interlayer coupling switched on, showing the hybridization of the two Dirac-Weyl cones.

stacking given by

$$H = \begin{pmatrix} \Delta & vp_x - ip_y & V_{\mathrm{AA}}(\mathbf{r}) & V_{\mathrm{AB}}(\mathbf{r}) \\ vp_x + ip_y & \Delta & V_{\mathrm{BA}}(\mathbf{r}) & V_{\mathrm{AA}}(\mathbf{r}) \\ V_{\mathrm{AA}}(\mathbf{r})^* & V_{\mathrm{BA}}(\mathbf{r})^* & -\Delta & vp_x - ip_y \\ V_{\mathrm{AB}}(\mathbf{r})^* & V_{\mathrm{AA}}(\mathbf{r})^* & vp_x + ip_y & -\Delta \end{pmatrix}, \tag{8}$$

where we have truncated the layer-diagonal blocks at linear order, which is convenient for the analytical work which follows. The diagonal blocks are thus Dirac-Weyl operators with valley index $v = \pm 1$, interlayer bias Δ, and the Fermi velocity set to unity. The interlayer potentials $V_{\mathrm{AB}}(\mathbf{r})$, $V_{\mathrm{BA}}(\mathbf{r})$, and $V_{\mathrm{AA}}(\mathbf{r})$ are the elements of the matrix given by Eq. (6). Through their spatial dependence these potentials can describe either a dislocation (Sec. VI) or an ideal or reconstructed twist bilayer (Sec. VII), while in Sec. III they will simply be constant potentials describing a rigid shift of the two layers. For the case of a partial dislocation these potentials are shown in the lower panel of Fig. 1, along with the components of corresponding relative shift vector $\Delta\mathbf{u}(x)$, upper panel.

III. FROM STACKING ORDER TO VALLEY CHERN INDEX

Analytical calculation of the Berry curvature of Eq. (8) would, for an arbitrary stacking, be opaquely complex. To simplify this problem we decompose the full Hamiltonian into two subsystems: a low energy sector spanned by the single layer states labeled 1 and 2 in Fig. 2 and a high energy sector spanned by states 3 and 4. These basis functions are just the eigenstates of Eq. (8) in the absence of interlayer coupling; note also that we consider the case $\Delta > 0$. The two basis sets are therefore

$$|\Psi_1^{(L)}\rangle = \frac{1}{\sqrt{2}}\begin{pmatrix} 1 \\ -ve^{iv\phi} \\ 0 \\ 0 \end{pmatrix} \qquad |\Psi_2^{(L)}\rangle = \frac{1}{\sqrt{2}}\begin{pmatrix} 0 \\ 0 \\ 1 \\ +ve^{iv\phi} \end{pmatrix} \tag{9}$$

for the low energy sector and

$$|\Psi_3^{(H)}\rangle = \frac{1}{\sqrt{2}}\begin{pmatrix} 1 \\ +ve^{iv\phi} \\ 0 \\ 0 \end{pmatrix} \qquad |\Psi_4^{(H)}\rangle = \frac{1}{\sqrt{2}}\begin{pmatrix} 0 \\ 0 \\ 1 \\ -ve^{iv\phi} \end{pmatrix} \tag{10}$$

for the high energy sector. In these expressions $\phi = \arctan(k_y/k_x)$ is the polar angle of the momentum. The justification for decomposing the full Hamiltonian in this way is that the Berry curvature will be associated with those parts of momentum space that, when the interlayer coupling is tuned to zero, have degenerate states. This is the physics captured by the low energy sector described by states 1 and 2. In calculating the Berry curvature for AB and BA stacking Zhang *et al.* [29] employed an alternative basis of states 1 and 4, calculating the Berry curvature deep in the valence band. We find that for the case of a general stacking this leads to an erroneous AA contribution to the topological invariant; apparently for the more general case a careful treatment of the low energy bands becomes important. As we will show, our result reproduces as a limit that of Ref. [29].

The low energy Hamiltonian in the basis of states 1 and 2 is

$$H^{\mathrm{low}} = \begin{pmatrix} \Delta - |k| & O \\ O^* & -\Delta + |k| \end{pmatrix} \tag{11}$$

while the high energy Hamiltonian in the basis of states 3 and 4 is given by

$$H^{\text{high}} = \begin{pmatrix} \Delta + |k| & -O \\ -O^* & -\Delta - |k| \end{pmatrix} \tag{12}$$

where in both cases the off-diagonal elements are given by

$$O = \frac{\nu}{2}(V_{\text{AB}} e^{\text{i}\nu\phi} - V_{\text{BA}} e^{-\text{i}\nu\phi}) =: |O| e^{\text{i}\theta}. \tag{13}$$

The ϕ dependent phase $\theta(\phi)$ will turn out to encode a layer dependent phase twist determining the valley Chern index. To bring this out we first diagonalize in the high and low energy sector finding for the eigenvalues

$$E^{\text{low}} = \pm\sqrt{(\Delta - |k|)^2 + |O|^2} =: \pm\xi, \tag{14}$$

and

$$E^{\text{high}} = \pm\sqrt{(\Delta + |k|)^2 + |O|^2} =: \pm\zeta \tag{15}$$

with the corresponding eigenvectors given by

$$|v_\pm^{\text{low}}\rangle = \frac{1}{\sqrt{2}} \begin{pmatrix} \sqrt{1 \pm \frac{\Delta - |k|}{\xi}} \\ \pm\sqrt{1 \mp \frac{\Delta - |k|}{\xi}}\, e^{-\text{i}\theta} \end{pmatrix} =: \begin{pmatrix} c_\pm \\ \pm c_\mp e^{-\text{i}\theta} \end{pmatrix} \tag{16}$$

and

$$|v_\pm^{\text{high}}\rangle = \frac{1}{\sqrt{2}} \begin{pmatrix} \sqrt{1 \pm \frac{\Delta + |k|}{\zeta}} \\ \pm\sqrt{1 \mp \frac{\Delta + |k|}{\zeta}}\, e^{-\text{i}\theta} \end{pmatrix} =: \begin{pmatrix} d_\pm \\ \pm d_\mp e^{-\text{i}\theta} \end{pmatrix}. \tag{17}$$

From these we can then reconstruct the wave functions in the original layer-sublattice space finding

$$|\Psi_\pm^{\text{low}}\rangle = \frac{1}{\sqrt{2}} \begin{pmatrix} c_\pm \\ -\nu e^{\text{i}\nu\phi} c_\pm \\ \pm c_\mp e^{-\text{i}\theta} \\ \pm\nu e^{\text{i}\nu\phi} c_\mp e^{-\text{i}\theta} \end{pmatrix} \tag{18}$$

and

$$|\Psi_\pm^{\text{high}}\rangle = \frac{1}{\sqrt{2}} \begin{pmatrix} d_\pm \\ +\nu e^{\text{i}\nu\phi} d_\pm \\ \pm d_\mp e^{-\text{i}\theta} \\ \mp\nu e^{\text{i}\nu\phi} d_\mp e^{-\text{i}\theta} \end{pmatrix}. \tag{19}$$

Note that for both the high and low energy sector for asymptotically large k different stacking types are related by the gauge transformation

$$|\Psi\rangle \to |\Psi\rangle\, e^{i(1-\tau_z)(\theta_1(\phi)-\theta_2(\phi))/2} \tag{20}$$

which, limiting to the two cases of AB or BA stacking for which $\theta = \mu\nu\phi$ [see Eq. (13)] with $\mu = \pm 1$ for AB and BA stacking, respectively, exactly recovers the gauge relation found in Ref. [29].

From these sublattice-layer space wave functions we can then determine the Berry connection $A_\pm^{\text{low/high}} = -\text{i}\,\langle\Psi_\pm^{\text{low/high}}\rangle\, \partial_\phi \Psi_\pm^{\text{low/high}}$, finding

$$A_\pm^{\text{low}} = \frac{1}{2}(\nu - c_\mp^2 \theta') \tag{21}$$

for the low energy sector and

$$A_\pm^{\text{high}} = \frac{1}{2}(\nu - d_\mp^2 \theta') \tag{22}$$

for the high energy sector, where $\theta' = \partial_\phi \theta$. The valley Chern number is defined as the integral over momentum space of the Berry curvature of the occupied bands. Summing the Berry connection over occupied states, i.e., $A = A_-^{\text{low}} + A_-^{\text{high}}$, we find

$$A = \nu - \theta' - \frac{\theta'}{2}\left(\frac{\Delta - |k|}{\xi} + \frac{\Delta + |k|}{\zeta}\right). \tag{23}$$

To ensure fully integrating the Berry curvature over momentum space we must integrate the connection on an asymptotically large contour around the K point, leading to the vanishing of the second bracketed term as both ξ and ζ reduce to $|k|$ as $|k| \to \infty$. We thus arrive at an expression for the Chern number given by

$$C = \nu - \frac{\theta(2\pi) - \theta(0)}{2\pi} \tag{24}$$

which depends only on the valley index $\nu = \pm 1$ and the winding number of O, Eq. (13). Expressing the generally complex interlayer potentials as their absolute value and phase, we define $V_{\text{AB}} = |V_{\text{AB}}| e^{i\theta_{\text{AB}}}$ and $V_{\text{BA}} = |V_{\text{BA}}| e^{-i\theta_{\text{BA}}}$, the equation for O can be written in polar coordinates as

$$\begin{aligned} O &= \frac{\nu}{2}[|V_{\text{AB}}| e^{\text{i}(\theta_{\text{AB}} + \nu\phi)} - |V_{\text{BA}}| e^{-\text{i}(\theta_{\text{BA}} + \nu\phi)}] \\ &= \frac{\nu}{2} e^{\text{i}\frac{\theta_{\text{AB}} - \theta_{\text{BA}}}{2}} [(|V_{\text{AB}}| - |V_{\text{BA}}|)\cos\tilde{\phi} \\ &\quad + \text{i}(|V_{\text{AB}}| + |V_{\text{BA}}|)\sin\tilde{\phi}] \end{aligned} \tag{25}$$

where the angle $\tilde{\phi}$ is given by

$$\tilde{\phi} = \nu\phi + \frac{(\theta_{\text{AB}} + \theta_{\text{BA}})}{2}. \tag{26}$$

Equation (25) describes an ellipse in the complex plane with turning direction determined by the relative sign between the sine and cosine terms. In the $\nu = +1$ valley we see that if $|V_{\text{AB}}| > |V_{\text{BA}}|$, the ellipse turns counterclockwise and the winding number is plus one while if $|V_{\text{AB}}| < |V_{\text{BA}}|$ it turns clockwise and the winding number is minus one; for the $\nu = -1$ valley, the situation is reversed. The valley Chern number for arbitrary stacking is therefore

$$C = \nu - \nu\ \text{sign}(|V_{\text{AB}}| - |V_{\text{BA}}|) \tag{27}$$

where the potentials V_{AB} and V_{BA} are related to the stacking through Eq. (6). From the Berry connection for AB and BA stacking derived in Ref. [29] one can obtain the corresponding formula $C = \nu(1 - \mu)$ for stacking types AB ($\mu = +1$) and BA ($\mu = -1$); evidently Eq. (27) reduces to this in the limit of considering only these stacking types. As one would expect, both these results vanish when summed over inequivalent valleys.

Employing the formalism of the previous section to obtain $|V_{\text{AB}}| - |V_{\text{BA}}|$ as a function of stacking vector $\Delta\mathbf{u}$ (see Sec. V for numerical details) the phase diagram of winding number versus stacking vector can be obtained and is shown in Fig. 3. A rather simple structure is observed in which the AA and SP structures (the structure midway between AB and BA

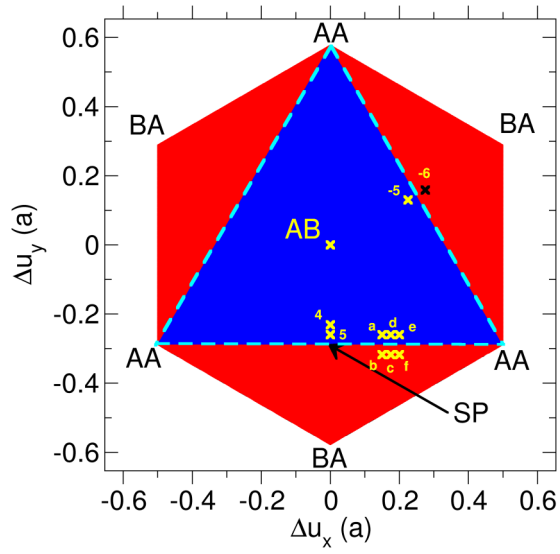

FIG. 3. Winding number phase diagram of bilayer graphene as a function of the relative shift of the two layers $\Delta\mathbf{u} = (\Delta u_x, \Delta u_y)$ (measured in units of the lattice constant a); red denotes a winding number of -1 and blue a winding number of $+1$. AB stacking corresponds to $\Delta\mathbf{u} = \mathbf{0}$, the center of the diagram, with BA and AA on the vertices. The stacking type SP is that found at a partial dislocation core and lies equidistant between AB and BA. The dashed lines are the "metal lines" on which the system remains metallic irrespective of the magnitude of the interlayer potential. The labeled crosses are the stacking vectors used to construct artificial domain walls to probe bound states associated with changing winding number; each panel in Fig. 5 corresponds to a pair of stacking vectors.

structures and found at the center of a partial dislocation) all lie on boundaries at which the valley Chern number changes.

IV. METALLIC LINES IN THE STACKING PHASE DIAGRAM

In a Gedanken experiment one can trace a path through this phase diagram by sliding two layers of graphene and so cross a boundary separating distinct topological invariants. On such a boundary the gap must therefore close irrespective of the magnitude of the interlayer potential. This thus represents a robust test of the valley Chern number diagram derived in the previous section: lines on which the valley Chern number changes must correspond to a permanent metallic state of the graphene bilayer for any interlayer potential.

To see that the lines separating regions of distinct topological invariants indeed correspond to "permanent metal lines" we calculate the band gap using the low energy Hamiltonian from the previous section. Its eigenvalues are

$$E = \pm\sqrt{(\Delta - |k|)^2 + |O|^2} \tag{28}$$

and so the gap minimum is at $|k| = \Delta$ and can only vanish on this circle for

$$O = \frac{1}{2}(V_{\mathrm{AB}}e^{\mathrm{i}\nu\phi} - V_{\mathrm{BA}}e^{-\mathrm{i}\nu\phi}) = 0. \tag{29}$$

Rewriting the potentials in polar form gives

$$|V_{\mathrm{AB}}|e^{\mathrm{i}(\nu\phi+\theta_{\mathrm{AB}})} = |V_{\mathrm{BA}}|e^{-\mathrm{i}(\nu\phi+\theta_{\mathrm{BA}})} \tag{30}$$

and so for the band gap to vanish at some momentum angle ϕ a necessary and sufficient condition is thus that the two potentials have the same magnitude, $|V_{\mathrm{AB}}| = |V_{\mathrm{BA}}|$. Note that just as in the calculation of the topological invariant the AA potential naturally drops out of the discussion, without artificially needing to be set to zero. The two complex numbers on either side of the equality are then identical for $\phi = -\nu(\theta_{\mathrm{AB}} + \theta_{\mathrm{BA}})/2$, from which $O = 0$ follows. To determine which stacking vectors this corresponds to, we employ the stacking potentials in the first star approximation which from Eq. (6) are found to be

$$V_{\mathrm{AB}} = t^{(0)}\left[1 + 2e^{-\frac{2\pi\mathrm{i}}{a}\Delta u_x}\cos\left(\frac{2\pi}{\sqrt{3}a}\Delta u_y\right)\right] \tag{31}$$

$$V_{\mathrm{BA}} = t^{(0)}\left[1 + 2e^{-\frac{2\pi\mathrm{i}}{a}\Delta u_x}\cos\left(\frac{2\pi}{\sqrt{3}a}\Delta u_y + \frac{2\pi}{3}\right)\right] \tag{32}$$

and insertion of these potentials in Eq. (30) then yields

$$\Delta u_y = \frac{\sqrt{3}a}{2}n + \frac{a}{\sqrt{3}} \tag{33}$$

$$\Delta u_y = \pm\sqrt{3}a\Delta u_x + \sqrt{3}am + \frac{a}{\sqrt{3}} \tag{34}$$

with $m, n \in \mathbb{Z}$. This corresponds precisely to the three lines on which the winding number changes sign. These "metallic lines" in the stacking phase diagram connect the regions of AA stacking and pass through the so-called "SP" structure that lies midway between AB and BA stacking. To numerically confirm this analytical result we display in Fig. 4 the gap as a function of stacking for interlayer bias of 0.2 eV and 1.0 eV; in both cases the gap can be seen to vanish on the metallic lines.

V. NUMERICAL METHOD

In order to probe both the veracity and consequences of the general relation between topological index and stacking order, Eq. (27), we now turn to numerical calculations. Our electronic structure calculations involve solving Eq. (8) numerically for both an analytical model of a single partial dislocation (see below) and for minimally twisted bilayer graphene, with the relaxed atomic structure obtained via semiempirical force field calculation. In what follows we describe our methodology for both electronic structure simulation and atomic relaxation; a complete description of method and numerical details can be found in Ref. [22].

A. Electronic structure calculations

We denote the relative shift in region i by $\Delta\mathbf{u}_i$ and model the displacement field around the boundary between different regions with the function

$$\Delta\mathbf{u}(x) = \mathbf{u}_1 + \frac{1}{2}(\mathbf{u}_2 - \mathbf{u}_1)\left(1 + \tanh\left(\frac{L(x - x_0)}{w}\right)\right) \tag{35}$$

that depends on three parameters; the location of the boundary x_0, its width w, and the length of the unit unit cell L. The vectors $\mathbf{u}_1$ and $\mathbf{u}_2$ are the shift of the two bulks either side of the dislocation relative to some reference structure. An illustration of the form of this domain wall model can be seen in Fig. 1 along with the corresponding interlayer potentials.

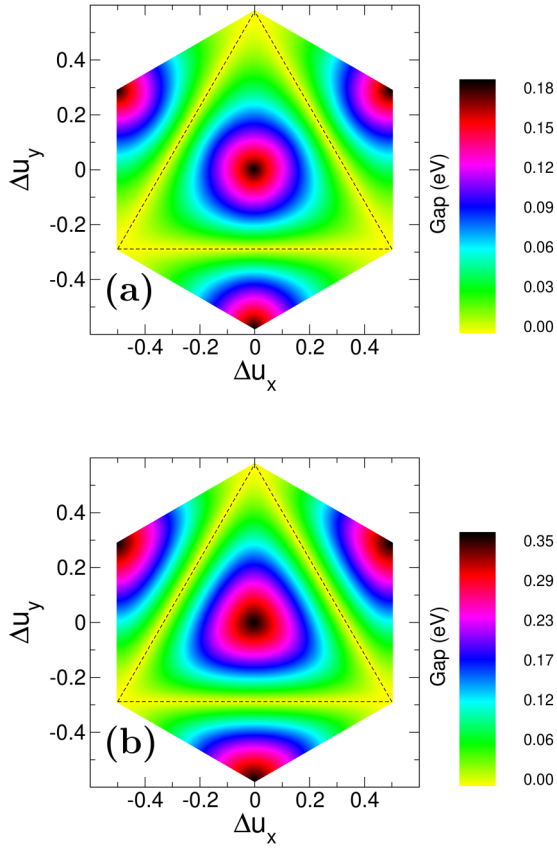

FIG. 4. The gap of bilayer graphene as a function of the relative shift of the two layers $\Delta\mathbf{u} = (\Delta u_x, \Delta u_y)$ (measured in units of the lattice constant a) and presented for two different values of the interlayer symmetry breaking potential: $\Delta = 0.2$ eV in panel (a) and $\Delta = 1.0$ eV in panel (b). On the lines at which the valley Chern number changes in the stacking phase diagram, Fig. 3, and illustrated by the dashed lines here, the gap remains zero irrespective of the interlayer bias applied.

As we employ periodic boundary conditions, we require two domain boundaries which we locate at $x_0 = 1/3$ and $x_0 = 2/3$ and for the sum of the partial Burgers vectors $(\mathbf{u}_2 - \mathbf{u}_1)$ for these two partial dislocations to sum to zero.

For the tight-binding method that underpins the continuum formalism we employ a π-band only approximation and take the in-plane and interlayer hopping functions to be parametrized by the same Gaussian form

$$t(\boldsymbol{\delta}) = Ae^{-B\delta^2} \tag{36}$$

with $A_\parallel$ and $B_\parallel$ are chosen to give an in-plane nearest neighbor hopping of 2.8 eV and the interlayer $A_\perp$ and $B_\perp$ chosen such that the hopping between nearest interlayer neighbors in the AB structure is 0.4 eV.

For numerical work we do not need to enforce a restriction to linear momentum (Dirac-Weyl approximation) and instead use a Hamiltonian in which the layer diagonal blocks are the full tight-binding description, with the layer off-diagonal blocks treated through Eq. (6):

$$H = \begin{pmatrix} H_{\mathrm{TB}}^{(1)} & S(x) \\ S^\dagger(x) & H_{\mathrm{TB}}^{(2)} \end{pmatrix}. \tag{37}$$

It is numerically efficient to use a basis of single layer eigenstates, determined from the layer diagonal blocks as [22]

$$H_{\mathrm{TB}}^{(n)} \left|\Psi_{i\mathbf{k}}^{(n)}\right\rangle = \epsilon_{i\mathbf{k}}^{(n)} \left|\Psi_{i\mathbf{k}}^{(n)}\right\rangle. \tag{38}$$

We find a basis size of 1600 of the lowest energy states from each layer provides good convergence for the low energy electronic structure of Eq. (37). In this basis the matrix elements of Eq. (37) are given by

$$[H]_{n'i'\mathbf{k}'ni\mathbf{k}} = \delta_{n'i'\mathbf{k}'ni\mathbf{k}}\epsilon_{i\mathbf{k}}^{(n)} + (1-\delta_{nn'})\left\langle\Psi_{i'\mathbf{k}'}^{(n')}\right| S(x) \left|\Psi_{i\mathbf{k}}^{(n)}\right\rangle. \tag{39}$$

B. Lattice relaxation

To calculate atomic relaxation we employ the GAFF force field [30] for the C-C interactions within the graphene layers and the registry-dependent interlayer potential of Kolmogorov-Crespi [31] using our own implementation [7,22]. For the ideal AB-stacked graphene bilayer this calculational setup results in an equilibrium lattice constant of $a_0 = 2.441$ Å and an interlayer distance of $d_{\mathrm{AB}} = 3.370$ Å. Shifting the graphene layers to AA stacking increases the layer separation to $d_{\mathrm{AA}} = 3.597$ Å (+0.227 Å as compared to AB stacking). The AA-stacked bilayer has a higher energy of 4.4 meV per atom as compared to AB stacking, corresponding to a stacking fault energy of $\gamma_{\mathrm{AA}} = 54.9$ mJ/m^2. In SP stacking order (see Fig. 3) the equilibrium distance of the graphene layers and the stacking fault energy are $d_{\mathrm{SP}} = 3.390$ Å (+0.020 Å) and $\gamma_{\mathrm{SP}} = 7.1$ mJ/m^2 (0.6 meV per atom), respectively, in excellent agreement with ACFDT-RPA calculations of Srolovitz *et al.* [32].

VI. PROBING THE PHASE DIAGRAM

We consider a model system consisting of a periodic unit cell with domain walls at $x = 1/3$ and $x = 2/3$ separating regions of stacking in the sequence $\Delta\mathbf{u}_1 \to \Delta\mathbf{u}_2 \to \Delta\mathbf{u}_1$ (here the vectors refer to the relative shift between the two layers). By choosing $\Delta\mathbf{u}_1$ and $\Delta\mathbf{u}_2$ to have either the same or different valley Chern numbers according to the phase diagram of Fig. 3, a robust test of the relation between valley Chern number and stacking vector can be performed. Note that the valley Chern number, being just the integral of the Berry curvature at one valley, can be defined for a single bilayer system of arbitrary stacking. As pointed out in Ref. [33] at best a marginal version of bulk-boundary correspondence exists for the valley Chern number since, as shown by these authors, it does not hold for the bilayer-vacuum interface. The goal of the present numerical investigation is thus to establish whether the difference of Chern numbers across a boundary between arbitrarily stacked bilayer graphene samples is robustly related to the existence of a boundary state. In Fig. 5 we show band structures that result from a representative set of choices of $\Delta\mathbf{u}_{1,2}$. The corresponding stacking vectors for each panel can be read off from the panel label and, as may be observed, in each case where $\Delta\mathbf{u}_{1,2}$ fall either side of a metal line, i.e., have different Chern numbers, gapless states are found in the spectrum. This thus establishes numerically bulk-boundary correspondence for arbitrarily stacked bilayer graphene samples.

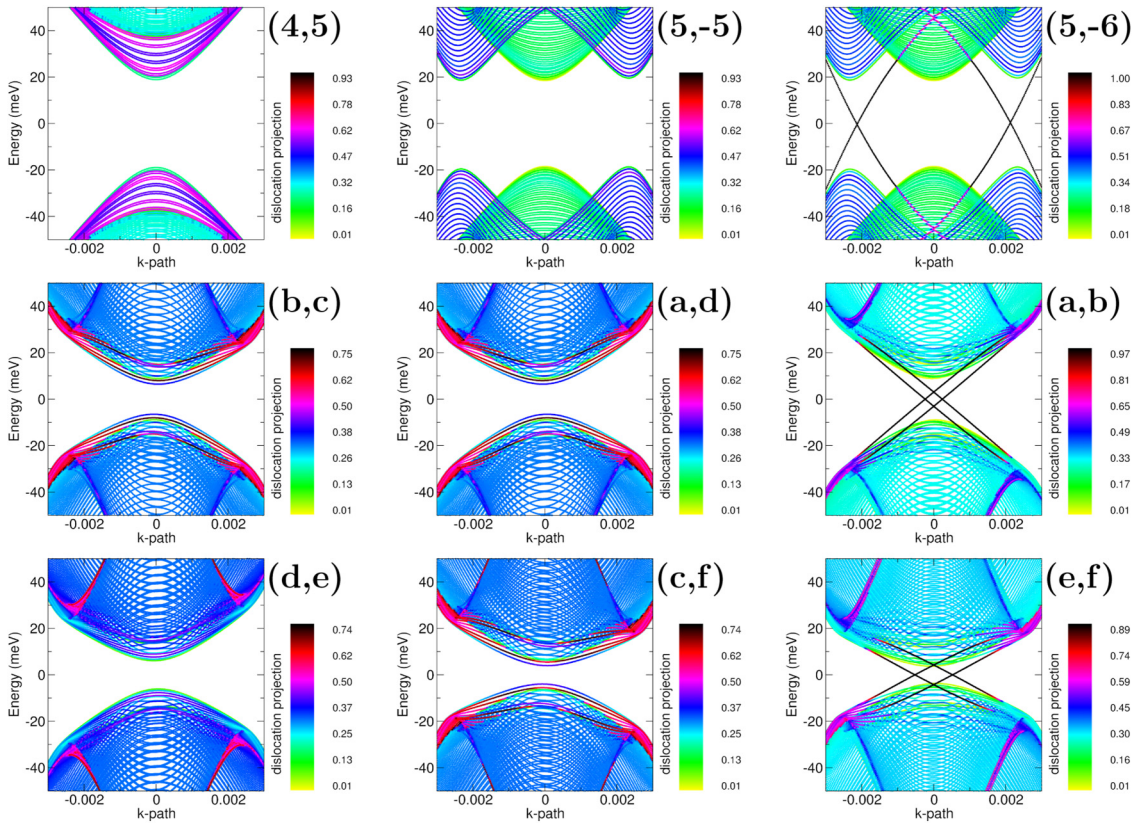

FIG. 5. Probing the topological phase diagram of bilayer graphene. Band structures for domain walls created between stacking types close to the "metal lines" of the stacking phase diagram separating regions of different valley Chern numbers. The labeling of each panel corresponds to the stacking vector either side of the domain wall, as indicated in Fig. 3, with the two stacking regions connected by a continuous change in stacking ("domain wall") given by Eq. (35) ($w = 50a$). The band structures in each row are almost identical, but in the third column gapless states appear. As can be seen from the phase diagram Fig. 3, in this column the stacking vectors fall either side of the metal line, and hence have different valley Chern numbers, while in the first two columns the stacking vectors fall on the same side of the metal line.

As a further numerical test, we probe the occurrence of bound states at nodes of the function $\text{sign}(|V_{\text{AB}}| - |V_{\text{BA}}|)$ in systems with smoothly modulated stacking potentials. We consider a unit cell $L = 10000a$ in which we have two partial dislocations at $x = 1/3$ and $x = 2/3$ separating regions of AB and BA stacking; the stacking sequence through the unit cell is thus AB→BA→AB, with the domain walls characterized by the partial Burgers vectors $(0, -\sqrt{2}/3)a$ and $(0, +\sqrt{2}/3)a$. A smooth stacking variation can then be obtained simply by allowing the partial width to become comparable to L. In Fig. 6 we see the band structures (left column) and squared wave functions and interlayer potentials (right column) for dislocation widths of $w = 50a$ (a realistic partial dislocation width), and $1000a$, $1250a$, and $1500a$. For the systems shown here we have taken $B_\perp = 4$, a fast decaying potential. This implies that for the misregistry of the layers seen within the core of partial dislocation a weak interlayer coupling, as for hopping vectors much greater in length than the minimal interlayer nearest neighbor separation the hopping matrix element quickly falls to zero. This is the reason for the overall weaker coupling seen at the center of the cell. While this decay is significantly faster than in bilayer graphene (the tight-binding fitting of Ref. [34] corresponds to $B_\perp = 0.43$) it generates the crossing of AB and BA potentials that we require for a numerical test of Eq. (27).

As can be seen from Fig. 6, as the sharp AB→BA→AB transition of the partial dislocation is broadened to a smooth modulation, an increasing number of states appear in the gap, which is almost closed for the $w = 1250a$ system. However, for each system there are two crossing points of the stacking potentials $|V_{\text{AB}}|$ and $|V_{\text{BA}}|$ and at each, as predicted by the change in topological index, bound states are seen in the right hand panel. [Note that to clearly associate the bound state with the crossing of $|V_{\text{AB}}|$ and $|V_{\text{BA}}|$ in panels (b), (d), and (h), we show a restricted view of a single crossing point.] For the $50a$ domain wall two right moving and two left moving linear gapless states very similar to those reported in the literature [34] can be seen; this is expected from bulk boundary correspondence as the difference in Chern number across the boundary is 2. As the dislocation broadens the gap fills with an increasing number of additional states. In each case, however, exactly at the crossing points of $|V_{\text{AB}}| - |V_{\text{BA}}|$ bound states are observed, fulfilling the expectation of Eq. (27). Note that all states in the gap of the pristine bilayer (100 meV) are shown in right hand panels, which accounts for the large number of states in each panel.

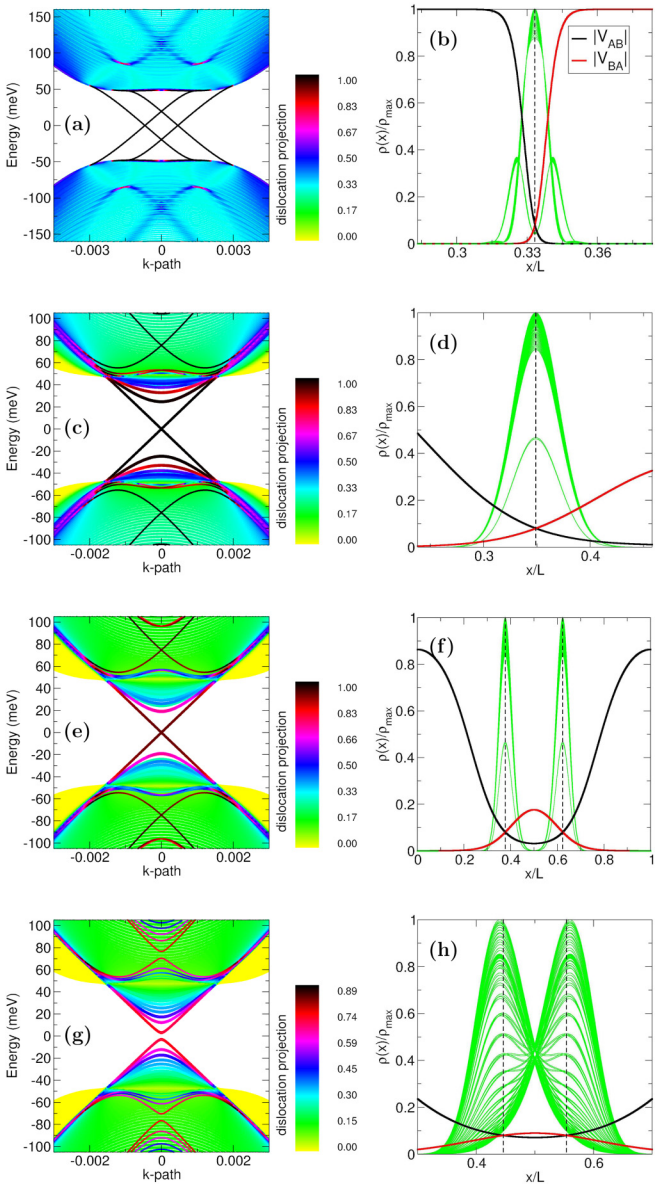

FIG. 6. Bound states at the crossing of V_{AB} and V_{BA} potentials. Left hand panels: Band structures for unit cells containing two boundaries (at $x/L = 1/3$, and $2/3$) with increasing dislocation widths of $50a$, $1000a$, $1250a$, and $1500a$ for panels (a), (c), (e), and (g), respectively. The length of the unit cell is $L = 10000a$. Right hand panels: The red and black lines indicate the corresponding V_{AB} and V_{BA} potentials. In panel (b) the potentials indicate a sharp domain wall connecting regions of AB and BA stacking, with a smooth stacking modulation as w increases, panel (f). The green lines are the square of the wave function for all states in the gap of the pristine bilayer (100 meV), see panel (a). Despite the increasingly smooth modulation, in all cases at the crossing of the V_{AB} and V_{BA} potentials is seen a series of pronounced bound states. [Note in panels (b), (d), and (h) a restricted region of the unit cell is shown for ease of identification of the correspondence of potential crossing with bound state).

VII. A CHERN INDEX MAP OF THE TWIST BILAYER

Having numerically tested the veracity of the relation between valley Chern number and stacking vector, we now address the question as to how the spatial variation of the valley Chern index is impacted by lattice relaxation in minimally twisted bilayer graphene. For the ideal twist bilayer (row 1 of Fig. 7, $\theta = 0.1^\circ$) the stacking potentials show an equal weight of AB, BA, and AA stacking types in the system (as they would for any three stacking projections which would produce a very similar picture but with potential maxima shifted off the high symmetry positions). Upon lattice relaxation this potential landscape dramatically alters: In row 2 we see that the AA potential has all but vanished, remaining only weakly visible at the dislocation core and nodes, with the AB and BA potentials describing a mosaic tiling with C_3 symmetry. Increasing the twist angle smooths the edges of this mosaic, and increases strength of the AA potential contribution, see row 3 of of Fig. 7 ($\theta = 0.33^\circ$) and row 4 ($\theta = 1.02^\circ$). The fourth and fifth columns of Fig. 7 display the difference $|V_{AB}| - |V_{BA}|$ and the winding number $\text{sign}(|V_{AB}| - |V_{BA}|)$. Remarkably, we see that the spatial variation of the winding number is identical for all systems. From the results of Secs. III and VI, this indicates that the formation of valley-momentum helical states, which is driven by the changing valley Chern number, will be impacted only in details by lattice relaxation.

To examine this we show in Fig. 8 the density of states and Fermi surfaces for a twist bilayer of $\theta = 1.02^\circ$ ($[p, q] = [1, 65]$ in the notation of Ref. [9]). While the density of states shows pronounced changes close to the Dirac point, the "valley" between the Dirac point peak and the two shoulder peaks remain largely unchanged. This low, almost constant DOS in the valley region corresponds to the gapless topological states, and as can be seen from the Fermi surfaces, Fig. 8(b), the details of this band structure remain qualitatively the same, with some increased hybridization due to relaxation opening the intersection points of the nested Fermi surface [particularly seen in Fig. 8(g)].

VIII. DISCUSSION

We have provided a general relation between the topological invariant of bilayer graphene and the stacking vector that describes mutual translation of the layers. We find that the Chern index is given by $C = \nu(1 - \text{sign}(|V_{AB}| - |V_{BA}|))$, with $|V_{AB}|$ and $|V_{BA}|$ the AB and BA components of the interlayer stacking potential. This generalizes the well known result that AB and BA stacked bilayer graphene have valley Chern numbers of 0 and 2 (for the K and K′ valley) and 2 and 0, respectively. A consequence of this generalization is that the valley Chern number is now associated with a condition on the interlayer fields rather than the fixed AB and BA structures, and this allows consideration of the occurrence of topologically protected states in regions of smooth stacking variation, such as moirés. As a numerical test of this we have performed simulations of artificially broadened domain walls finding bound states at the crossing of the $|V_{AB}|$ and $|V_{BA}|$, as would be expected due to the change in value of C at this point.

With this tool in hand we have examined the valley Chern number for minimally twisted bilayer graphene, finding that the underlying spatial dependence of the valley Chern index is, essentially, independent of atomic relaxation. The

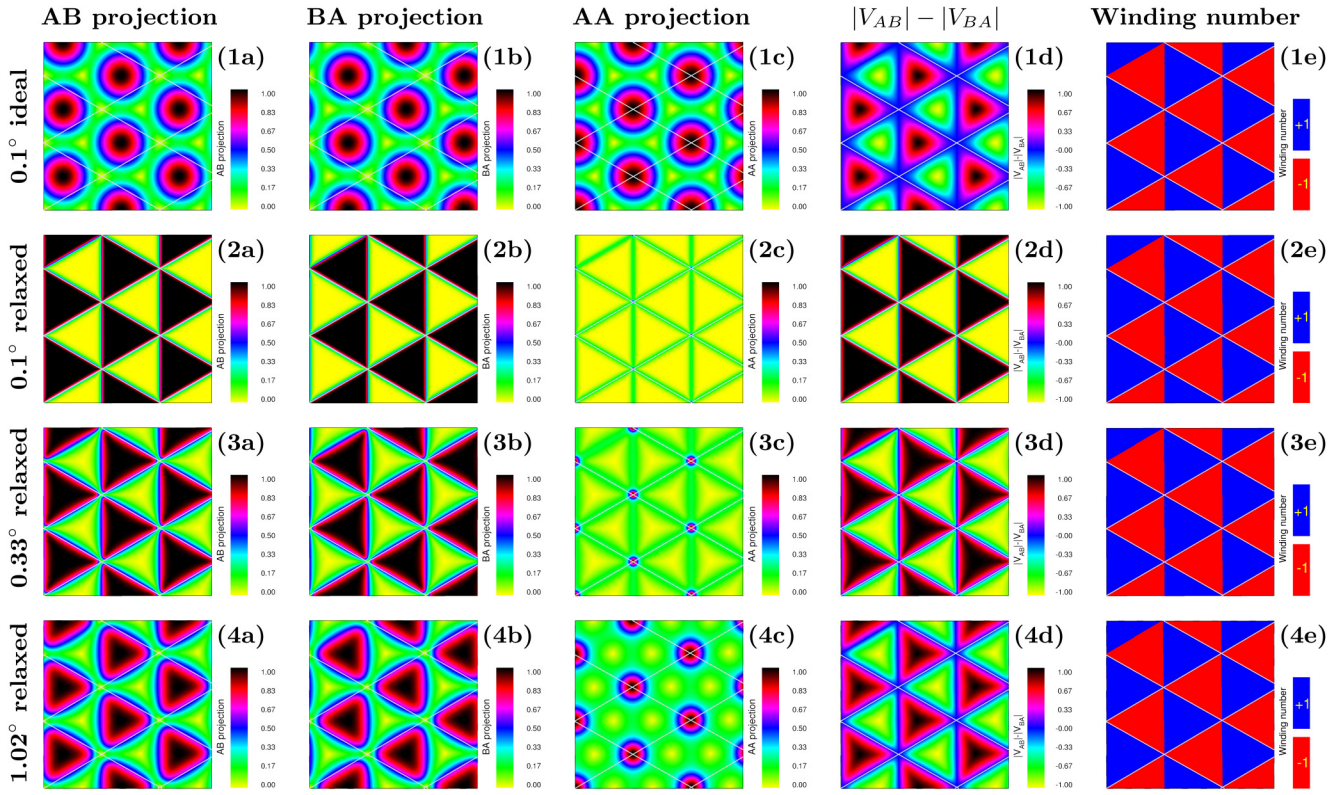

FIG. 7. Stacking order and Chern index of the twist bilayer. In columns (a)–(c) are shown the absolute values of the V_{AB}, V_{BA}, and V_{AA} potentials of a series of twist bilayers. The ideal twist bilayer for $\theta = 0.1^\circ$ ($[p, q] = [1, 661]$ in the notation of Ref. [9] with 1 310 764 atoms in the unit cell) is shown in panels 1(a)–1(c), and a similar picture would be found for any angle. In rows 2–4 the stacking potentials for the relaxed twist bilayer at twist angles of 0.1°, 0.33°, ($[p, q] = [1, 199]$, 118 804 atoms) and 1.02° ($[p, q] = [1, 65]$, 12 676 atoms) are displayed. Evidently, at small angles the ideal and relaxed structures appear to be two completely different materials. The difference of $|V_{\mathrm{AB}}| - |V_{\mathrm{BA}}|$, however, exhibits a closer resemblance between the different systems [panels 1(d)–4(d)], and the sign of this difference, which determines the valley Chern number, is essentially identical for all systems [panels 1(e)–4(e)].

topological physics of this material, in particular helical network states, is thus qualitatively similar in the ideal and relaxed twist bilayer. In fact, the ideal twist geometry can be expected to have a much "cleaner" manifestation of the helical network due to the reduced scattering as the interlayer coupling contains only three (first star) momentum boosts,

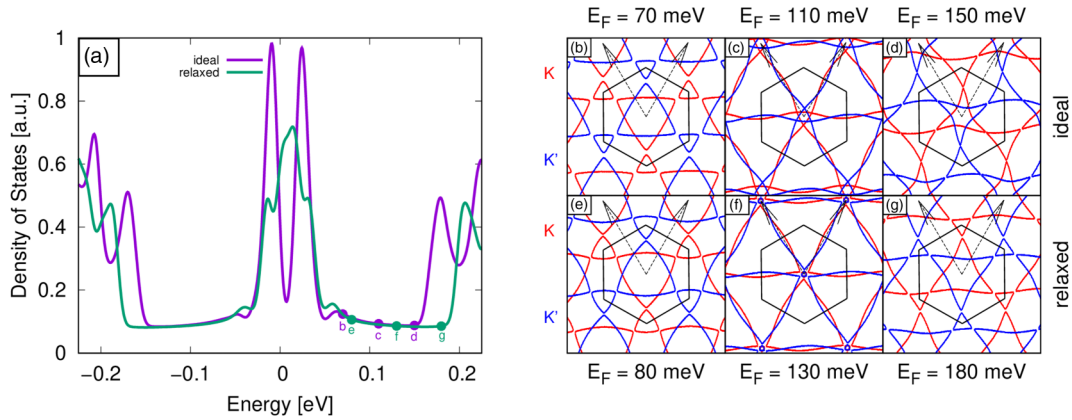

FIG. 8. Density of states and Fermi surfaces for relaxed and unrelaxed minimally twisted bilayer graphene for a twist angle of $\theta = 1.02^\circ$ in an applied bias of $V = 200$ meV. Left hand panel: While the density of states changes significantly close to the Dirac point upon atomic relaxation, the low DOS region between the Dirac point and shoulder peaks remains very similar. Right hand panel: This robustness to relaxation extends to the Fermi surfaces, which upon relaxation exhibit hybridization at the intersection of the nested Fermi lines and some change in the nesting vector, but remain qualitatively the same in both ideal and relaxed structures. Note that the energies at which the Fermi surfaces are evaluated are scaled so that they correspond to the same relative position between the Dirac and shoulder peaks.

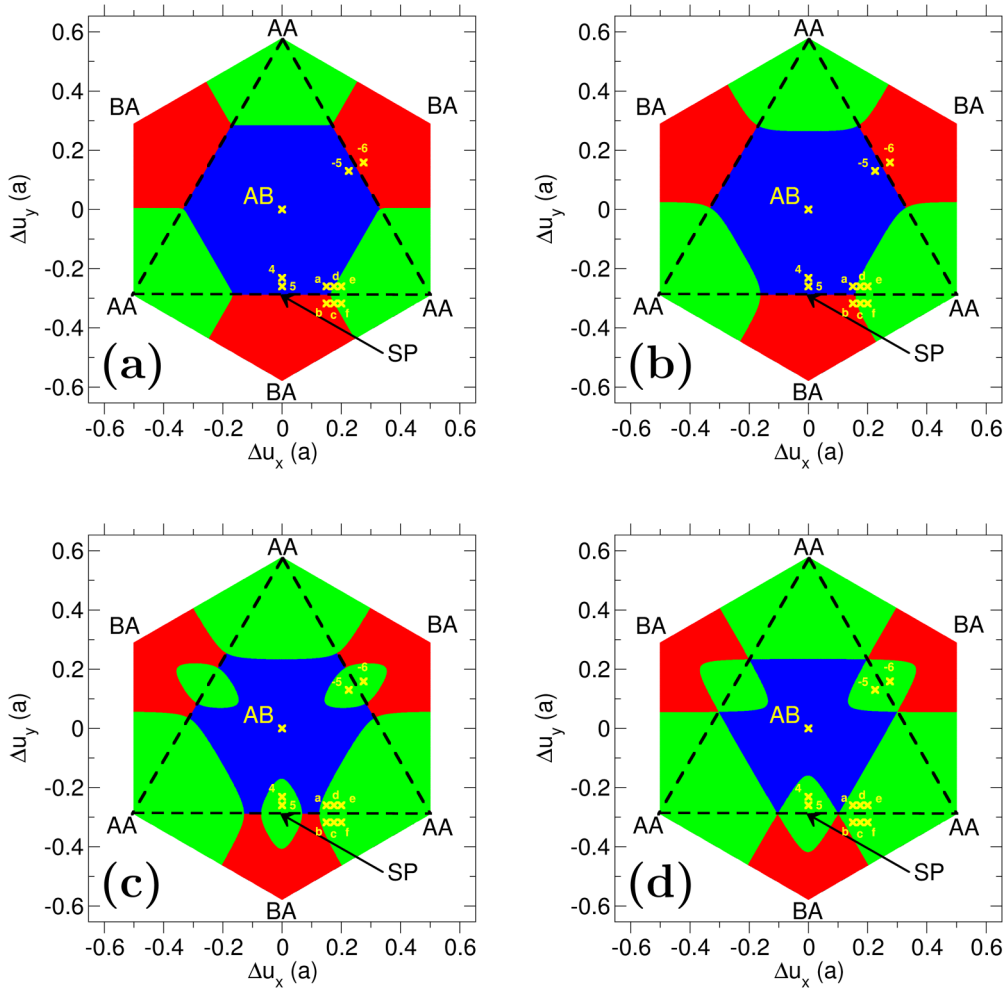

FIG. 9. Phase diagrams obtained from using eigenstates 1 and 4 from Fig. 2 as the basis for deriving the auxiliary Hamiltonian used in calculation of the Berry connection for arbitrarily stacked bilayer graphene. This choice generates an erroneous dependence of the valley Chern number on the relative strengths of the AA stacking part of the interlayer coupling, the V_{AA} potential, and the AB/BA stacking part of the interlayer coupling, V_{AB} and V_{BA}, see Eq. (A7). The relative strengths of these potentials is, in turn, determined by the range of the interlayer coupling; in the interlayer tight-binding form $t_\perp = A_\perp e^{-B_\perp \delta^2}$ B takes on values 12.0, 4.0, 0.6, and 0.1 in panels (a)–(d), respectively, within each case the value of $A_\perp$ is chosen such that the direct interlayer coupling (i.e., for atoms coincident in the x-y plane) is 0.4 eV. This corresponds to a change from a very short range interlayer interaction [panel (a)] to a soft longer range interlayer interaction, panel (d).

as opposed to the continuum of momentum boosts of the dislocation network.

ACKNOWLEDGMENTS

The work was carried out in the framework of the SFB 953 "Synthetic Carbon Allotropes" (Project Number 182849149) of the Deutsche Forschungsgemeinschaft (DFG). F.W. thanks the Graduate School GRK 2423 (DFG, Project Number 377472739) for financial support. S.S. and S.S. acknowledge the funding of the DFG, reference SH 498/4-1.

APPENDIX: CALCULATION WITH INCORRECT V_{AA} CONTRIBUTION

As mentioned in the main text, performing the calculation of Sec. III with eigenstates 1 and 4 from Fig. 2 generates an erroneous V_{AA} contribution to the Chern number. Here we present this calculation.

Projecting the Hamiltonian from Eq. (8) onto these basis states yields the single auxiliary Hamiltonian

$$H^{\mathrm{aux}} = \begin{pmatrix} \Delta - |k| & O \\ O^* & -\Delta - |k| \end{pmatrix} \tag{A1}$$

with the off-diagonal elements given by

$$O = V_{\mathrm{AA}} - \frac{\nu}{2}(V_{\mathrm{AB}} e^{\mathrm{i}\nu\phi} + V_{\mathrm{BA}} e^{-\mathrm{i}\nu\phi}). \tag{A2}$$

Note that the form of the auxiliary Hamiltonian off-diagonal potential, O, has changed here as compared to the result obtained in Sec. III. In particular the "occupied bands" basis employed here yields a dependence of O on the AA stacking potential not found when using the full basis, see Eq. (13). The matrix in Eq. (A1) has eigenvalues

$$E = -|k| \pm \sqrt{\Delta^2 + |O|^2} =: -|k| \pm \xi \tag{A3}$$

and eigenvectors

$$v_{\pm} = \frac{1}{\sqrt{2}} \begin{pmatrix} \sqrt{1 \pm \frac{\Delta}{\xi}} \\ \pm\sqrt{1 \mp \frac{\Delta}{\xi}} e^{i\theta} \end{pmatrix} =: \begin{pmatrix} c_{\pm} \\ \pm c_{\mp} e^{i\theta} \end{pmatrix}. \tag{A4}$$

We construct new states in a four-dimensional space via $|\Psi_{\pm}\rangle = v_{\pm,1}|\Psi_1\rangle + v_{\pm,2}|\Psi_4\rangle$ and from these the Berry connection

$$A_{\pm} = -i\langle\Phi_{\pm}|\partial_{\phi}\Phi_{\pm} = \frac{1}{2}\left(\nu - \theta' \pm \frac{\theta'}{\xi}\right) \tag{A5}$$

can be obtained. Tracing over the two occupied bands and integrating around a fixed k path we end up with the valley Chern number

$$C = \nu - \frac{\theta(2\pi) - \theta(0)}{2\pi}. \tag{A6}$$

This is formally equivalent to the result given in the main text. However, the valley Chern number is defined through the winding number of the off-diagonal elements of the Hamiltonian Eq. (A1). In contrast to the off-diagonal elements given by Eqs. (11) and (12) of the main text, we now have a plus sign between the V_{AB} and V_{BA} terms and an additional V_{AA} term. The plus sign does not affect the winding number, however, if the V_{AA} term becomes sufficiently large, the off-diagonal term O will no longer encircle the origin during the angular integral, leading to zero winding number. The winding number is thus only nonzero if

$$|V_{AA}| < \frac{1}{2}[(|V_{AB}| + |V_{BA}|)^2 \cos^2\tilde{\phi} + (|V_{AB}| - |V_{BA}|)^2 \sin^2\tilde{\phi}]^{\frac{1}{2}}. \tag{A7}$$

Numerical investigation of dependence of this valley Chern number on stacking shows that the phase diagram depends on the range of the interlayer coupling (which determines the strength of the AA stacking potential V_{AA}). As can be seen in Fig. 9 as the interaction range increases, from a very short range interaction in panel (a) to a longer range interaction in panel (d), the magnitude of V_{AA} compared to that of the AB/BA potentials increases and the patches of zero winding number grow. If correct, this would imply that the existence of boundary states would depend on the particular form of the interlayer coupling, and no such dependence has been found in our numerical calculations.

[1] S. Dai, Y. Xiang, and D. J. Srolovitz, Twisted bilayer graphene: Moiré with a twist, Nano Lett. **16**, 5923 (2016).

[2] S. K. Jain, V. Jurii, and G. T. Barkema, Structure of twisted and buckled bilayer graphene, 2D Materials **4**, 015018 (2016).

[3] H. Yoo, R. Engelke, S. Carr, S. Fang, K. Zhang, P. Cazeaux, S. H. Sung, R. Hovden, A. W. Tsen, T. Taniguchi, K. Watanabe, G.-C. Yi, M. Kim, M. Luskin, E. B. Tadmor, E. Kaxiras, and P. Kim, Atomic and electronic reconstruction at the van der Waals interface in twisted bilayer graphene, Nat. Mater. **18**, 448 (2019).

[4] F. Gargiulo and O. V. Yazyev, Structural and electronic transformation in low-angle twisted bilayer graphene, 2D Materials **5**, 015019 (2017).

[5] N. N. T. Nam and M. Koshino, Lattice relaxation and energy band modulation in twisted bilayer graphene, Phys. Rev. B **96**, 075311 (2017).

[6] J. S. Alden, A. W. Tsen, P. Y. Huang, R. Hovden, L. Brown, J. Park, D. A. Muller, and P. L. McEuen, Strain solitons and topological defects in bilayer graphene, Proc. Natl. Acad. Sci. U.S.A. **110**, 11256 (2013).

[7] B. Butz, C. Dolle, F. Niekiel, K. Weber, D. Waldmann, H. B. Weber, B. Meyer, and E. Spiecker, Dislocations in bilayer graphene, Nature (London) **505**, 533 (2014).

[8] S. Shallcross, S. Sharma, E. Kandelaki, and O. A. Pankratov, Electronic structure of turbostratic graphene, Phys. Rev. B **81**, 165105 (2010).

[9] S. Shallcross, S. Sharma, and O. Pankratov, Emergent momentum scale, localization, and van Hove singularities in the graphene twist bilayer, Phys. Rev. B **87**, 245403 (2013).

[10] G. T. de Laissardière, D. Mayou, and L. Magaud, Localization of dirac electrons in rotated graphene bilayers, Nano Lett. **10**, 804 (2010).

[11] R. Bistritzer and A. H. MacDonald, Moire bands in twisted double-layer graphene, Proc. Natl. Acad. Sci. U.S.A. **108**, 12233 (2011).

[12] D. Weckbecker, S. Shallcross, M. Fleischmann, N. Ray, S. Sharma, and O. Pankratov, Low-energy theory for the graphene twist bilayer, Phys. Rev. B **93**, 035452 (2016).

[13] P. San-Jose and E. Prada, Helical networks in twisted bilayer graphene under interlayer bias, Phys. Rev. B **88**, 121408(R) (2013).

[14] D. K. Efimkin and A. H. MacDonald, Helical network model for twisted bilayer graphene, Phys. Rev. B **98**, 035404 (2018).

[15] P. Lucignano, D. Alfè, V. Cataudella, D. Ninno, and G. Cantele, Crucial role of atomic corrugation on the flat bands and energy gaps of twisted bilayer graphene at the magic angle 1.8°, Phys. Rev. B **99**, 195419 (2019).

[16] M. Angeli, D. Mandelli, A. Valli, A. Amaricci, M. Capone, E. Tosatti, and M. Fabrizio, Emergent D_6 symmetry in fully relaxed magic-angle twisted bilayer graphene, Phys. Rev. B **98**, 235137 (2018).

[17] S. G. Xu, A. I. Berdyugin, P. Kumaravadivel, F. Guinea, R. K. Kumar, D. A. Bandurin, S. V. Morozov, W. Kuang, B. Tsim, S. Liu, J. H. Edgar, I. V. Grigorieva, V. I. Fal'ko, M. Kim, and A. K. Geim, Giant oscillations in a triangular network of one-dimensional states in marginally twisted graphene, Nat. Commun. **10**, 4008 (2019).

[18] B. Tsim, N. N. T. Nam, and M. Koshino, Perfect one-dimensional chiral states in biased twisted bilayer graphene, Phys. Rev. B **101**, 125409 (2020).

[19] C. De Beule, F. Dominguez, and P. Recher, Aharonov-Bohm Oscillations in Minimally Twisted Bilayer Graphene, Phys. Rev. Lett. **125**, 096402 (2020).

[20] S. Huang, K. Kim, D. K. Efimkin, T. Lovorn, T. Taniguchi, K. Watanabe, A. H. MacDonald, E. Tutuc, and B. J. LeRoy, Topologically Protected Helical States in Minimally Twisted Bilayer Graphene, Phys. Rev. Lett. **121**, 037702 (2018).

[21] P. Rickhaus, J. Wallbank, S. Slizovskiy, R. Pisoni, H. Overweg, Y. Lee, M. Eich, M.-H. Liu, K. Watanabe, T. Taniguchi, T. Ihn, and K. Ensslin, Transport through a network of topolog-

ical channels in twisted bilayer graphene, Nano Lett. **18**, 6725 (2018).

[22] M. Fleischmann, R. Gupta, F. Wullschläger, S. Theil, D. Weckbecker, V. Meded, S. Sharma, B. Meyer, and S. Shallcross, Perfect and controllable nesting in minimally twisted bilayer graphene, Nano Lett. **20**, 971 (2020).

[23] F. Rost, R. Gupta, M. Fleischmann, D. Weckbecker, N. Ray, J. Olivares, M. Vogl, S. Sharma, O. Pankratov, and S. Shallcross, Nonperturbative theory of effective Hamiltonians for deformations in two-dimensional materials: Moiré systems and dislocations, Phys. Rev. B **100**, 035101 (2019).

[24] R. Gupta, F. Rost, M. Fleischmann, S. Sharma, and S. Shallcross, Straintronics beyond homogeneous deformation, Phys. Rev. B **99**, 125407 (2019).

[25] F. Kisslinger, C. Ott, C. Heide, E. Kampert, B. Butz, E. Spiecker, S. Shallcross, and H. B. Weber, Linear magnetoresistance in mosaic-like bilayer graphene, Nat. Phys. **11**, 650 (2015).

[26] S. Shallcross, S. Sharma, and H. B. Weber, Anomalous dirac point transport due to extended defects in bilayer graphene, Nat. Commun. **8**, 342 (2017).

[27] D. Weckbecker, R. Gupta, F. Rost, S. Sharma, and S. Shallcross, Dislocation and node states in bilayer graphene systems, Phys. Rev. B **99**, 195405 (2019).

[28] R. Gupta, S. Maisel, F. Rost, D. Weckbecker, M. Fleischmann, H. Soni, S. Sharma, A. Görling, and S. Shallcross, Deformation induced pseudomagnetic fields in complex carbon architectures, Phys. Rev. B **100**, 085135 (2019).

[29] F. Zhang, A. H. MacDonald, and E. J. Mele, Valley Chern numbers and boundary modes in gapped bilayer graphene, Proc. Natl. Acad. Sci. U.S.A. **110**, 10546 (2013).

[30] J. Wang, Romain M. Wolf, J. W. Caldwell, P. A. Kollman, and D. A. Case, Development and testing of a general amber force field, J. Comput. Chem. **25**, 1157 (2004).

[31] A. N. Kolmogorov and V. H. Crespi, Registry-dependent interlayer potential for graphitic systems, Phys. Rev. B **71**, 235415 (2005).

[32] S. Zhou, J. Han, S. Dai, J. Sun, and D. J. Srolovitz, van der waals bilayer energetics: Generalized stacking-fault energy of graphene, boron nitride, and graphene/boron nitride bilayers, Phys. Rev. B **92**, 155438 (2015).

[33] J. Li, A. F. Morpurgo, M. Büttiker, and I. Martin, Marginality of bulk-edge correspondence for single-valley hamiltonians, Phys. Rev. B **82**, 245404 (2010).

[34] C. Lee, G. Kim, J. Jung, and H. Min, Zero-line modes at stacking faulted domain walls in multilayer graphene, Phys. Rev. B **94**, 125438 (2016).